

COSMOCR: A Numerical Code for Cosmic Ray Studies in Computational Cosmology

Francesco Miniati

*Max-Planck-Institut für Astrophysik, Karl-Schwarzschild-Str. 1, D-85741
Garching, Germany*

*School of Physics and Astronomy, University of Minnesota, Minneapolis, MN
55455*

Abstract

We present COSMOCR, a numerical code for the investigation of cosmic ray related studies in computational cosmology. The code follows the diffusive shock acceleration, the mechanical and radiative energy losses and the spatial transport of the supra-thermal particles in cosmic environment. Primary cosmic ray electrons and ions are injected at shocks according to the thermal leakage prescription. Secondary electrons are continuously injected as a results of p-p inelastic collisions of primary cosmic ray ions and thermal background nuclei. The code consists of a conservative, finite volume method with a power-law sub-grid model in momentum space. Two slightly different schemes are implemented depending on the stiffness of the cooling terms. Comparisons of numerical results with analytical solution for a number of tests of direct interest show remarkable performance of the present code.

Key words:

1 Introduction

Structure formation is a major research area in cosmology and a powerful observational constraint to discriminate among the viable cosmological models [1]. For example, the evolution of the larger structures such as Galaxy Clusters, being very sensitive to the underlying mass content of the Universe, is used to evaluate the density parameter Ω_m for matter [2,3]. Numerical simulations have proven an invaluable tool and have qualitatively confirmed our theoretical framework for the mechanism of structure formation [4]. Today, in the era of high precision cosmology, a substantial part of the efforts are directed toward the development of a coherent and quantitative picture. This must be inclusive

of the feedback from forming structure (e.g., stars, galaxies, and active galactic nuclei), which strongly affects the evolution of the observable universe.

In this context, cosmic-ray (CR hereafter) pressure has been recently recognized as a possible source of significant dynamical feedback [5]. Indeed, during the hierarchical process of structure formation, supersonic gas in-fall and merging events invariably generate powerful, large and long-lived shock waves [6–9]. These should produce copious amounts of CRs, by way of diffusive shock acceleration [10], including both electrons and ions. In addition, the post-shock gas and diffusively trapped CRs are mostly advected into non-expanding regions, such as filaments and clusters. It turns out that the energy of most of the CR-protons is only marginally affected by radiative losses during a Hubble time. It is possible, then, that the latter might accumulate inside large forming structures, storing up a substantial fraction of the total pressure there [11]. In addition to cosmic shocks other sources of CRs are also possible. These include active galactic nuclei, supernovae and stellar winds, all of which are candidate for important contributions to the total population of CRs in cosmic structures [12]. There is growing observational evidence that significant non-thermal activity takes place in clusters of galaxies. This evidence is provided by extended sources of radio emission, namely radio halos and relics. From its spectral properties and, sometimes, polarization signatures the radio emission is interpreted as synchrotron radiation, implying the presence of relativistic cosmic-ray electrons and magnetic fields [13–17]. Also, there have been claims of detection of radiation in excess to what is expected from the hot, thermal X-ray emitting intra cluster medium, both in the hard X-ray band above ~ 10 KeV [18,19] and perhaps even in the extreme ultra-violet [20–26]. The importance of this non-thermal component and its cosmological implications will be discussed elsewhere [27,28].

In this paper we describe a numerical code that allows a treatment of the evolution of various CR populations (i.e., protons as well as primary and secondary electrons) in computational cosmology. This code is instrumental for a detailed investigation of the aforementioned issues connected with the non-thermal activity associated with the formation of the large scale structure. In §2 we outline the difficulty of the numerical treatment of CRs in this context and a strategy for useful applications. The code is extensively described in §3. There we present the algorithm for the treatment of CR ions and electrons including their advection in both momentum (§§3.1, 3.2) and physical space (§3.4). In addition we describe the inclusion of two source mechanisms, namely injection at shocks (§3.5) and production of secondary electrons (§3.6). Finally, in §4 we present some numerical experiments to test the code performance.

2 Challenges and Approach

The evolution of the supra-thermal particles, i.e., CR electrons and ions is described by the diffusion-convection equation [29]. In comoving coordinates the latter takes the form

$$\begin{aligned} \frac{\partial f}{\partial t} = & -\frac{1}{a} \mathbf{u} \cdot \nabla f + \frac{1}{a^2} \nabla(\kappa \nabla f) \\ & + \frac{1}{a} \left(\dot{a} + \frac{1}{3} \nabla \cdot \mathbf{u} \right) p \frac{\partial f}{\partial p} + \frac{1}{p^2} \frac{\partial}{\partial p} \left(p^2 \left[b_\ell(p) f + D_p \frac{\partial f}{\partial p} \right] \right) + \\ & + j(\mathbf{x}, p). \end{aligned} \quad (1)$$

where the gradient is with respect to comoving coordinates, \mathbf{x} , $a(t)$ is the expansion parameter of the universe (such that $\mathbf{r} = a\mathbf{x}$ is the physical length), $\mathbf{u} = a(t)\dot{\mathbf{x}}$ is the peculiar velocity (i.e., not inclusive of the Hubble expansion) and $f(\mathbf{x}, p)$ is the isotropic part of the particle distribution function in comoving units. Here $\kappa(p)$ and $D_p(p)$ are the diffusion coefficients in comoving coordinates and momentum space, respectively. We recall that on the right-hand side of the above equation, the first line contains the spatial terms of advection and diffusion respectively; the second line includes the adiabatic losses due to cosmic ($\propto \dot{a}$) and peculiar ($\propto \nabla \cdot \mathbf{u}$) expansion, other mechanical and radiative losses [$\propto b_\ell(p)$; see eq. (3.7)] and the second-order Fermi mechanism ($\propto D_p$); and the third line [$j(\mathbf{x}, p)$] represent the comoving source term, which accounts for either fresh CRs injection at shock or secondary production. Eq. (1) holds only for sub-horizon scales and, more importantly, in the non-relativistic limit. These approximations are completely satisfactory for the investigations of the problems outlined in the introduction. On the other hand, shock acceleration in relativistic flows such as those occurring in relativistic jets, gamma-ray bursts and the like, needs to be treated differently [30–32].

The acceleration and transport of CR electrons and ions, described by the above equation, involve physical scales that must be carefully considered when a numerical approach is undertaken. The major difficulty arises in the attempt to model the behavior of supra-thermal particles nearby shocks. There, the smallest length scale of interest is that of the shock thickness, ℓ_s , which, for a collision-less shock, is typically of order a few times the Larmor radius of a thermal proton [33,34], i.e.,

$$\ell_s \sim r_L \sim \frac{pc}{ZeB} \sim \left(\frac{T}{10^8 \text{K}} \right) \left(\frac{B}{0.1 \mu\text{G}} \right)^{-1} 10^{11} \text{ cm}. \quad (2)$$

Here T is the post-shock temperature and B is the magnetic field strength.

Particles injected at shocks are thought to be pulled out from the high energy tail of the thermal pool and have energy and a Larmor radius a few times above the thermal values [35–39]. At even higher energy, CRs have a Larmor radius much larger than the shock thickness and, therefore, unlike the thermal particles, are unaffected by the local shock transition. In the vicinity of a shock the dynamics of these supra-thermal particles is dominated by the effects of advection and diffusion, which determine the energy gain and escape probability for the particles [40]. In particular, the spatial distribution is characterized by a diffusive scale-length $\lambda_d(p) = \kappa(p)/u_s$ (where u_s is the shock velocity), which determines the distance upstream of the shock to which a particle can propagate by diffusing against the advective flow. For a correct numerical solution of eq. (1), the hierarchy of the aforementioned scale lengths for all relevant momentum, namely that $\ell_s < \lambda_d(p) \lesssim \lambda_d(p_{max})$, must be properly reproduced in the numerical grid [41]. This demands a full resolution of the diffusion length, typically $\Delta x \lesssim \lambda_d/10$, as the shock discontinuity is usually spread over 2-3 grid zones in a numerical simulation. When this spatial resolution is achieved, the physical roles of diffusion and advection in eq. (1) are well accounted for, and the property of continuity of the complete distribution function, at the shock surface can be reproduced [40]. Notice that the continuity of the distribution function across the shock (in the shock frame), justified by the fact that the supra-thermal particles do not experience the discontinuity, is the very condition that determines the power law behavior of the solution $f(\mathbf{x}, p)$ emerging from a shock wave [40]. Otherwise, the finite, numerical size of the shock, Δx_s , induces an error in the solution of eq. (1) of order $\Delta x_s/\lambda_d$ [41].

However, resolving spatial scales down to the sub-diffusion length of the supra-thermal particles turns out to be an extremely demanding task. In fact, if we assume for simplicity the case of Bohm diffusion, $\kappa = \kappa_B = \frac{1}{3}r_L v$, with r_L and $v \sim c$, the particle Larmor radius and velocity, respectively, we find

$$\lambda_d(p) = \frac{\kappa_B(p)}{u_s} = 1.1 \left(\frac{E}{\text{GeV}} \right) \left(\frac{B}{0.1 \mu\text{G}} \right)^{-1} \left(\frac{u_s}{10^2 \text{Km s}^{-1}} \right)^{-1} 10^{-2} \text{ pc.} \quad (3)$$

where $E \simeq \text{pc}$ is the particle energy (in the relativistic limit) and u_s is the shock speed. This means that for electrons with energy $\lesssim 1\text{--}10 \text{ GeV}$, which are of interest for the non-thermal emission in galaxy clusters, the diffusion length is $\lesssim 10^{-2} \text{ pc}$ and should be even smaller at injection energies. Considered the importance of including the cosmic structure on a scale $\gtrsim 50 h^{-1} \text{ Mpc}$ [42], the spatial scales to be resolved extend over more than 10 orders of magnitude! Therefore, we can typically only afford grid sizes $\Delta x \gg \lambda_d(p)$ and following the full dynamics of the CRs injection and acceleration at cosmological shocks becomes impractical. However, although limited by the above restrictions, one can still attempt to find a useful numerical treatment of the CR particles. In

particular, the instance that $\lambda_d(p)/\Delta x \ll 1$ also implies that the diffusion time at shocks, $\tau_d(p) = \lambda_d/u_s \leq (\lambda_d(p)/\Delta x) \Delta t \ll \Delta t$, i.e., much smaller than the computational time-step [41]. The diffusive shock acceleration time, τ_{acc} , for a strong shock ($r \equiv u_1/u_2 \simeq 4$) is

$$\begin{aligned} \tau_{acc}(p) &= \frac{3}{u_1 - u_2} \left(\frac{\kappa_1}{u_1} + \frac{\kappa_2}{u_2} \right) = 3r \left(\frac{r+1}{r-1} \right) \frac{\kappa(p)}{u_1^2} \simeq 20 \tau_d(p) \\ &= 21.1 \left(\frac{E}{\text{GeV}} \right) \left(\frac{B}{0.1 \mu\text{G}} \right)^{-1} \left(\frac{u_s}{10^2 \text{Km s}^{-1}} \right)^{-1} \text{ yr} \end{aligned} \quad (4)$$

where r is the shock compression ratio, subscripts 1 and 2 indicate values upstream and downstream of the shock, respectively, and for simplicity we have assumed $\kappa_1 = \kappa_2$. Since the time-step for a cosmological simulation is of order of 10^8 yr, with the above representative values of magnetic field strength and shock speed, $\Delta t \gg \tau_{acc}$ up to a CR energy $E \simeq 10^{15}$ eV. This energy is well beyond the range of energies of interest for CR electrons in clusters of galaxies and should include most of the CR ions dynamically relevant in those environments. In fact at energies much larger than that, both energy losses [43] and diffusive escape [11] become important reducing the population of CRs with $E \gtrsim 10^{15}$ eV. Thus, for both CR electrons and ions within the energy range derived above, we will assume that shock acceleration is *instantaneous* [36,44] and that a downstream steady-state solution is generated in accord with the properties of the shock [41]. The simplest way to implement this prescription (*acceleration*) is to “inject” in correspondence of shock fronts a test particle distribution of CRs (cf. [40])

$$f(p) = f_{inj} \left(\frac{p}{p_{inj}} \right)^{-q_s} \quad (5)$$

where the slope is given by

$$q_s = \frac{3r}{r-1}. \quad (6)$$

Here the injection momentum p_{inj} is determined by the post-shock temperature (see in §3.5 for details.) In addition, when a pre-existing population of CRs, $f_0(p)$, encounters a shock, the particle distribution is modified (*re-acceleration*) only if the log-slope of the current distribution, $q_0 = -\partial \ln f_0 / \partial \ln p$, is larger than that determined by the shock compression ratio [eq. (6)] (cf. [40]). In general, the injected and re-accelerated particle distributions could also be affected by the nonlinear feed-back of the CRs themselves [45]. In this case the distribution function deviates from the simple power-law given in eq.(5).

Once the supra-thermal particles have been produced at shocks, they are carried through “smooth” flows together with the background gas (before another encounter with a shock). The circumstance that $\lambda_d \ll \Delta x$ suggests that over the scale Δx of the numerical grid, the propagation of the particles is dominated by the advection term. In fact, the relative contribution of advection and diffusion in eq. (1) is of order $k/u_s \Delta x = \lambda_d/\Delta x \ll 1$. Thus, for the spatial transport of the CR particles in shock-less regions, the diffusion term is negligible and can be dismissed in eq. (1) [41].

3 The Cosmic Rays Code

3.1 Advection in Momentum Space

The difficulty of a numerical treatment of eq. (1) is aggravated by the fact in practice we are allowed to use only a “handful” of grid zones in momentum space. To illustrate, in the hypothesis that the number of grid zones used for the one-dimension momentum variable is the same as for the spatial variables, a N^4 single precision array for a CR population would require already about 17Gb for $N = 256$. The number of operations to be computed at each cycle grows consequently ($\propto N^4$) which is paid at the high cost of a low speed code. Finally, we must not forget that the data-set output by the simulation becomes huge, rendering the post-computation analysis memory intensive and difficult to handle even on well equipped workstations.

With only a few grid zones spanning the momentum space, a sub-grid model of the distribution function is necessary. For this purpose, in the following we adopt the general approach first developed in ref. [41], although some aspects of the implementation of the numerical schemes below are different from those authors. In particular we compute the flux in momentum space exactly up to a logarithmic term and provide an alternative scheme for the stiff losses case. We sub-divide the region of p -space of interest into N_p logarithmically spaced momentum *bins*, bounded by p_0, \dots, p_{N_p} . The width of the bins is expressed on a log scale as $\Delta \log p \equiv \Delta w_i = \log(p_i/p_{i-1})$, which is convenient (although not necessary) to take as constant. On this grid, we approximate $f(p)$ with the following piece-wise power law:

$$f(p) = f_i \left(\frac{p}{p_{i-1}} \right)^{-q_i} \quad (7)$$

where f_i and q_i are the normalization and logarithmic slope for the i th momentum bin. This approximation is valid when $q(p)$ changes slowly inside each

bin, which holds true as long as energy losses do not produce strong curvature in the distribution function $f(p)$. Then, integration over the i_{th} momentum bin of eq. (1) multiplied by a factor $4\pi p^2$, gives

$$\begin{aligned} \frac{\partial n_i}{\partial t} = & -\frac{1}{a} \nabla \cdot (\mathbf{u} n_i) + \frac{1}{a^2} \nabla (\langle \kappa \rangle \nabla n_i) + \\ & + \frac{1}{a} \left\{ \left[\left(\dot{a} + \frac{1}{3} \nabla \cdot \mathbf{u} \right) p + a \left(b_\ell(p) + D_p \frac{\partial \log f}{\partial p} \right) \right] 4\pi p^2 f(p) \right\}_{p_{i-1}}^{p_i} + \\ & + Q_i \end{aligned} \quad (8)$$

where

$$n_i = \int_{p_{i-1}}^{p_i} 4\pi p^2 f(p) dp = 4\pi f_i p_{i-1}^3 \frac{\left(\frac{p_i}{p_{i-1}}\right)^{3-q_i} - 1}{3 - q_i} \quad (9)$$

$$\langle \kappa \rangle_i = \frac{\int_{p_{i-1}}^{p_i} p^2 \kappa \nabla f dp}{\int_{p_{i-1}}^{p_i} p^2 \nabla f dp} \quad (10)$$

$$Q_i = \int_{p_{i-1}}^{p_i} 4\pi p^2 j(p) dp; \quad (11)$$

and where we have used eq. (7) to derive the expression (9). As already pointed out, away from shocks we can neglect the diffusive term. Furthermore, we henceforth drop the second order Fermi term and focus on the solution of the equation

$$\frac{\partial n_i}{\partial \tau} = -\nabla \cdot (\mathbf{u} n_i) + [b(p) 4\pi p^2 f(p)]_{p_{i-1}}^{p_i} + Q_i \quad (12)$$

where $\tau = t/a$ and we have introduced

$$b(p) \equiv - \left(\frac{dp}{d\tau} \right)_{tot} = \left(\dot{a} + \frac{1}{3} \nabla \cdot \mathbf{u} \right) p + a b_\ell(p) \quad (13)$$

which includes, in addition to other energy loss terms ($b_\ell(p)$; see §3.7), the adiabatic terms due to cosmic expansion and fluid divergence (convergence). For the sake of clarity, we shall address now separately the details regarding the integration of each term of eq. (12). To begin with, we will focus on the contribution due to advection in momentum space responsible for the change

$$\frac{\partial n_i}{\partial \tau} = [b(p) 4\pi p^2 f(p)]_{p_{i-1}}^{p_i} \quad (14)$$

Time integration of eq. (14) yields

$$n_i^{\tau+\Delta\tau} - n_i^\tau = -\Delta\tau (\Phi_i^p - \Phi_{i-1}^p) \quad (15)$$

where

$$\Phi_i^p = -\frac{1}{\Delta\tau} \int_{\tau}^{\tau+\Delta\tau} b(p) 4\pi p^2 f(\tau', p) |_{p_i} d\tau', \quad (16)$$

is the time-averaged flux and the integrand is evaluated at the cell boundary p_i . Recalling eq. (7), the above integration is readily carried out after using eq. (13) to rewrite it as

$$\Phi_i^p = \frac{4\pi}{\Delta\tau} \int_{p_i}^{p_u} p^2 f_j(p) dp \quad (17)$$

where

$$j = \begin{cases} i+1 & \text{if } b(p_i) > 0 \\ i & \text{if } b(p_i) \leq 0 \end{cases} \quad (18)$$

and p_u is the upstream momentum, solution of the integral equation

$$\Delta\tau = - \int_{p_i}^{p_u} \frac{dp}{b(p)} \quad (19)$$

After updating n_i based on (15), and including the contributions from spatial advection and injections (detailed below), the sub-grid model of the distribution function (7) is reconstructed by solving for f_i and q_i at each computational cell. For each new value n_i , f_i and q_i are related by eq. (9), so one additional constraint is necessary. For the second relation we assume that the curvature of the spectrum is constant, i.e., $q_{i+1} - q_i = q_i - q_{i-1}$ (cf. [41] for more detail on this). This is a sensible approximation when cooling is weak. It is, therefore, very suitable for cosmic ray ions, which, in a cosmological context and for the energy range of interest here, suffer only minor losses even during a Hubble time. However, for the case of electrons, which cool much more rapidly, this approximation breaks down and additional measures must be taken, which we address below.

3.2 Alternative Scheme for Fast Cooling Electrons

The assumption of a smooth CR energy distribution (constant spectrum curvature), which allows one to infer the slope of the distribution function from the particle number density in each bin, breaks down in the presence of strong cooling. This is an important issue for electrons, since the cooling times associated with inverse Compton and synchrotron losses are much shorter than the time-scale of a cosmological simulation. It is important to notice that the effect of strong inverse Compton or synchrotron cooling is that of producing a cut-off in the particle distribution, not just a mere steepening of it. Since each momentum bin spans a considerable range of values, it is often the case that the cut-off falls in the middle of a bin, so that only the part of the bin below the energy cut-off is populated, while upper part is completely depleted. This situation is likely to occur for any of the momentum bins, not just those at the highest energies, because, due to additional Coulomb losses (see §3.7), the cooling times for the electrons at all energies of interest are always smaller than or comparable to the Hubble time. For the same reason, except around shocks where they are continually injected, primary CR electrons in most of the simulated volume only occupy a very few of the lower energy momentum bins. This adds a non-trivial complication because at least three momentum bins are necessary for the reconstruction scheme mentioned in the previous section to work [41].

In order to circumvent these difficulties, we have devised an alternative scheme to be employed for the electrons only. The idea consists of replacing the “constant curvature” assumption with a different condition that allows us to reconstruct both normalization, f_i , and slope, q_i , of the piecewise power-law distribution function (7) in each bin. A natural constraint is provided by the physical condition that the total energy be conserved, except for the explicit sources and sinks. The corresponding equation is derived by taking one *moment* of the transport equation (1). Thus, after multiplying by a factor $4\pi p^2 T(p)$, where $T(p) = (\gamma - 1) m_e c^2$ is the particle kinetic energy (where $\gamma = 1/\sqrt{1 - (v/c)^2}$ is Lorentz factor), and integrating over the i_{th} momentum bin, we have

$$\begin{aligned}
\frac{\partial \varepsilon_i}{\partial t} = & -\frac{1}{a} \nabla \cdot (\mathbf{u} \varepsilon_i) + \frac{1}{a^2} \nabla \cdot (\langle \kappa_{\mathbf{T}} \rangle_i \nabla \varepsilon_i) \\
& + \frac{1}{a} \left\{ \left[\left(\dot{a} + \frac{1}{3} \nabla \cdot \mathbf{u} \right) p + a b_\ell(p) \right] 4\pi p^2 f(p) T(p) \right\}_{p_{i-1}}^{p_i} \\
& - \frac{1}{a} \int_{p_{i-1}}^{p_i} \left[\left(\dot{a} + \frac{1}{3} \nabla \cdot \mathbf{u} \right) p + a b_\ell(p) \right] 4\pi p^2 f(p) \frac{p}{\sqrt{m_e^2 c^2 + p^2}} dp \\
& + S_i.
\end{aligned} \tag{20}$$

As before, we have dropped the second order Fermi term, and introduced the following definitions

$$\varepsilon_i = \int_{p_{i-1}}^{p_i} 4\pi c p^2 f(p) T(p) dp = 4\pi c f_i p_{i-1}^4 \frac{\left(\frac{p_i}{p_{i-1}}\right)^{4-q_i} - 1}{4 - q_i} \quad (21)$$

$$\langle \kappa_T \rangle_i = \frac{\int_{p_{i-1}}^{p_i} \kappa p^2 (\nabla f) T(p) dp}{\int_{p_{i-1}}^{p_i} p^2 (\nabla f) T(p) dp} \quad (22)$$

$$S_i = \int_{p_{i-1}}^{p_i} 4\pi p^2 j(p) T(p) dp, \quad (23)$$

where eq. (7) has been used and the sub-relativistic contribution has been ignored in order to derive the last expression in eq. (21). The first two terms on the right hand side of eq. (20) represent the usual spatial advection and diffusion respectively. The third and fifth terms account for advection in momentum space and external energy source respectively, analogous to the corresponding third and fourth terms in eq. (8). Finally, in the fourth term on the right hand side we combine, for reasons of numerical convenience, both the CR pressure and the sink contributions.

As before, the diffusion term can be neglected, whereas both spatial advection and energy injection will be treated in the next sections. The changes affecting the distribution in momentum space are then provided by the third and fourth terms according to

$$\frac{\partial \varepsilon_i}{\partial \tau} = \left[b(p) 4\pi p^2 f(p) T(p) \right]_{p_{i-1}}^{p_i} - \int_{p_{i-1}}^{p_i} b(p) \frac{4\pi p^3 f(p)}{\sqrt{m_e^2 c^2 + p^2}} dp, \quad (24)$$

where $\tau = t/a$ and $b(p)$ is defined by (13). For the range of energy of interest here $p \gg m_e c$. Then, by using the prescription in (7) for $f(p)$, the second term in eq. (24) can be rewritten as $\varepsilon_i R_i(q_i, p_{i-1})$, where:

$$R_i(q_i, p_{i-1}) = \int_{p_{i-1}}^{p_i} b(p) \frac{p^{3-q_i}}{\sqrt{m_e^2 c^2 + p^2}} dp \quad / \quad \int_{p_{i-1}}^{p_i} p^{2-q_i} T(p) dp. \quad (25)$$

Thus, after integration over a time-step eq. (24) reads

$$\varepsilon_i^{\tau+\Delta\tau} \left(1 + \frac{\Delta\tau}{2} R_i \right) = \varepsilon_i^\tau \left(1 - \frac{\Delta\tau}{2} R_i \right) - \Delta\tau \left(\Phi_i^\varepsilon - \Phi_{i-1}^\varepsilon \right) \quad (26)$$

where the term $\propto R_i$ has been integrated implicitly and

$$\Phi_i^\varepsilon = -\frac{1}{\Delta\tau} \int_{\tau}^{\tau+\Delta\tau} b(p) 4\pi p^2 f_i(\tau', p) T(p) |_{p_i} d\tau', \quad (27)$$

is the time-averaged flux whose integrand part is evaluated at the cell boundary p_i . In analogy with the previous section, by using the definition (7) and eq. (13) the above integral is readily rewritten as

$$\Phi_i^\varepsilon = \frac{4\pi}{\Delta\tau} \int_{p_i}^{p_u} p^2 f_j(p) T(p) dp \quad (28)$$

where the index j and the upper integration limit, p_u , are defined in (18) and (19) respectively. In addition, the maximum momentum of the electrons distribution, p_{cut} , is followed explicitly by means of equation (13), which can be easily integrated analytically [46] for the cooling mechanisms of interest here. Therefore, in this scheme in eq. (28) and eq. (17) we adopt the minimum between p_u and p_{cut} . Following explicitly the value of p_{cut} , i.e., the high energy cut-off of the distribution, allows us to describe the electrons in the last momentum bin by a normalization and slope appropriate for the still populated portion of that bin.

After accounting for the advection in physical space and source terms treated in the following sections, we have information on both the particle number density and kinetic energy at each momentum bin. Taking the ratio of energy to number density for each bin, we find for $p_i \gg mc$.

$$\frac{\varepsilon_i}{n_i p_{i-1} c} = \frac{3 - q_i}{\left(\frac{p_i}{p_{i-1}}\right)^{3-q_i} - 1} \frac{\left(\frac{p_i}{p_{i-1}}\right)^{4-q_i} - 1}{4 - q_i} \quad (29)$$

which can be solved in the unknown q_i through Newton-like method with only a few iterations. The value of f_i , which is actually not explicitly needed in any integration step, can easily be computed from either definition (9) or (21). In this method both f_i and q_i are derived from quantities pertaining exclusively to the i_{th} bin and no information about the adjacent bins is required. Thus the scheme works with even one single cell or a fraction of it (since we keep track of p_{cut} which can even be smaller than p_1). This allows us to follow for cosmological times the low energy electrons with $\gamma \sim 300$. The electrons in this energy range have the longest lifetime against energy losses in a cosmological environment [47]. Thus, about 10^9 yr after a CR distribution has been produced in a shock, these are the only electrons left. However, It is important to keep track of them, even if most of the electrons at higher or lower energy have been

depleted, because they can contribute to the extreme ultra-violet radiation detected in clusters of galaxies.

3.3 Constraint on the Time-step

In order for the scheme described in §3.1 and §3.2 to behave properly the time step $\Delta\tau$ must be such that $|\log \frac{p_u}{p_i}| \leq \epsilon_{CFL} \Delta w$ where $\epsilon_{CFL} \leq 1$ is a Courant-like number. Given the very long cooling times for the proton CRs compared to the typical cosmological time-step, there is no need to enforce the above condition for this case. For the electrons, however, we find that in order to follow accurately the evolution near the high energy cut-off a limit on the time-step $\Delta\tau \lesssim 0.1\tau_{sync+IC}$ should be adopted.

3.4 Advection in Physical Space

While we have focused so far almost exclusively on the integration of the diffusion-convection equation in momentum space, the full evolution of the CR particles must also include the effects of spatial transport. Since we neglect the spatial diffusion for reasons already pointed out in §2, the main contribution in this respect is provided by the advection terms. In eq. (12) and (20), these are of the form

$$\frac{\partial c_i}{\partial \tau} = -\nabla \cdot (\mathbf{u} c_i) \quad (30)$$

with $c_i = n_i$ or ε_i respectively. These terms are integrated by means of a van Leer method [48], which is a conservative, second order accurate and Total Variation Diminishing scheme. The scheme allows integration of the advection terms in one dimension and the full integration along all three different directions is achieved by directional splitting [49]. As a general feature of conservative, Godunov-like schemes [50], the quantity that is being updated is the volume-average over the computational cell ¹, i.e.,

$$\bar{c} = \frac{\int_V c(\mathbf{x}) d^3x}{\int_V d^3x} = \frac{1}{V} \int_V c(\mathbf{x}) d^3x \quad (31)$$

The time update is accomplished through a double integration of eq. (30) over the cell volume and over the time-step Δt . Upon performing such integrations,

¹ We point out, for the sake of completeness, that because of this volume-averaging step, the distribution function f employed in §3.2 should be read as \bar{f} , i.e., its volume average.

we find

$$\bar{c}_i^{\tau+\Delta\tau} - \bar{c}_i^\tau = -\Delta\tau \sum_{\ell=1,2,3} (\Phi_{x_\ell}^x - \Phi_{x_{\ell-1}}^x) \quad (32)$$

where the index ℓ runs over the three spatial coordinates and accounts for the flux through the computational cell boundaries along the three spatial directions. The time-averaged flux in physical space is defined as

$$\Phi_{x_\ell}^x = \frac{1}{\Delta t \Delta x} \int_t^{t+\Delta t} c_i u_\ell |_{x_\ell} dt' \quad (33)$$

with the integrand evaluated at the cell boundaries x_ℓ . The numerical solution $c(t, \mathbf{x}, p)$ is reconstructed from the volume average values (\bar{c}) as a piecewise linear interpolation. An important part of this step is the effort to restrict the slopes of the linear interpolation. In fact, having the potential to become artificially large near extrema or discontinuities, they can cause unwanted oscillations and render the scheme unstable. This problem is eliminated by demanding that the interpolated function is monotone [48]. The reconstructed solution can then be upgraded “exactly” in Lagrangian coordinates as $c(t', \mathbf{x}, p) = c(t, \mathbf{x} - \int_t^{t'} \mathbf{v} dt, p)$, allowing the calculation of the flux in eq. (33) at each interface x_ℓ .

3.5 Injection

The source terms in eq. (12) and (20) are responsible for the variations

$$\bar{n}_i^{\tau+\Delta\tau} - \bar{n}_i^\tau = Y_i \quad (34)$$

$$\bar{\varepsilon}_i^{\tau+\Delta\tau} - \bar{\varepsilon}_i^\tau = \Sigma_i \quad (35)$$

respectively, where

$$Y_i = \frac{1}{V \Delta t} \int_t^{t+\Delta t} \int_V Q_i d^3x dt = \frac{1}{\Delta t} \int_t^{t+\Delta t} \bar{Q}_i dt \quad (36)$$

$$\Sigma_i = \frac{1}{V \Delta t} \int_t^{t+\Delta t} \int_V S_i d^3x dt = \frac{1}{\Delta t} \int_t^{t+\Delta t} \bar{S}_i dt \quad (37)$$

$$(38)$$

and Q_i and S_i have been defined by eq. (11) and (23), respectively. In this section, we shall focus our attention on source contributions provided by CR

injection at shocks. With this term we indicate the number of particles that upon passing through a shock are assumed to undergo the diffusive shock acceleration mechanism. Since the latter is treated as instantaneous, injection here basically refers to the deposition in the post-shock region of CRs with a power-law distribution in momentum space which accords with the diffusive shock acceleration theory (see §2) for further details). Next (§3.6), we will outline the scheme for the injection term due secondary electrons produced in inelastic p-p collisions.

The scheme described here for the injection of CRs at shocks is based on the *thermal leakage* model which seems to be observationally supported at least by *in situ* measurements at the earth bow shock [35]. Here, we assume that upon passing through the shock most of the gas thermalizes to a Maxwellian distribution with post-shock temperature T_2 , i.e.,

$$f_m(p) = n_2 (2m_p k T_2)^{-3/2} \exp\left(-\frac{p^2}{2m_p k T_2}\right) \quad (39)$$

with n_2 the total number of particles of the distribution. For a particle to return upstream it is necessary not only that it propagates faster than the shock wave, but also that it has enough energy to escape “trapping” by Alfvén waves generated in the downstream turbulence [51,52]. Thus, only those particles in the high energy tail of the thermal distribution will have a chance to re-cross the shock and get injected into the acceleration mechanism. The numerous, complicated details of the physics underlying the injection mechanism are conveniently modeled by a few parameters [37–39,53]. One of them, c_1 , defines the momentum threshold for the particles of the thermal distribution to be injected, as

$$p_{inj} = c_1 2\sqrt{m_p k T_2}. \quad (40)$$

In practice we assume that at p_{inj} the thermal distribution, $f_m(p_{inj})$ [eq. (39)], joins “smoothly” into the power-law distribution of the CRs. That implies

$$f_{cr}(p) = f_m(p_{inj}) \left(\frac{p}{p_{inj}}\right)^{-q}, \quad (41)$$

where $q = 3r/(r - 1)$, r is the shock compression ratio and $p_{inj} \leq p \leq p_{max}$. With these choices, c_1 is the only free parameter in the injection model. In fact, the total number of injected particles is given by

$$n_{inj} = \int_{p_{inj}}^{\infty} 4\pi p^2 f_{cr}(p) dp = 4\pi f_m(p_{inj}) p_{inj}^3 \frac{\left(\frac{p_{max}}{p_{inj}}\right)^{3-q} - 1}{3 - q}. \quad (42)$$

and the injection efficiency, i.e., the fraction of downstream thermal gas particles that are injected in the acceleration process, is [cf. eq. (39) and (40)]

$$\eta_{inj} \equiv \frac{n_{inj}}{n_2} = 8 \sqrt{\frac{2}{\pi}} c_1^3 e^{-2c_1^2} \frac{\left(\frac{p_{max}}{p_{inj}}\right)^{3-q} - 1}{3-q}, \quad (43)$$

practically independent of T_2 . In an alternative approach, where the downstream gas distribution is not specified, η_{inj} and c_1 can be taken as independent parameters [38,45]. With the above setting, CR particles are injected per unit shock surface at a rate

$$\bar{Q}_i = \eta_{inj} \frac{\rho_1 u_s}{m_p} = \eta_{inj} \frac{n_2 u_2}{r} \quad (44)$$

where $n_2 u_2 = n_1 u_1$ is the number flux of thermal particles impinging on the shock. Given the injection rate, \bar{Q}_i , and the distribution of the injected particles in eq. (41), the energy injection term, S_i , can be easily computed as well by means of eq. (23).

The actual values of c_1 and η_{inj} are not known and most likely they are not constant, but a function of the conditions of the flow. For ionic CRs, observations at the earth's bow shock indicate that an injection efficiency, η_{inj} , can be as high as 1.25×10^{-3} [54] or even $\sim 10^{-2}$ [35]. In theoretical studies of shock acceleration at supernova remnants the parameter c_1 is assumed in the range 2.3-2.5 corresponding to values of η_{inj} ranging between a few $\times 10^{-3}$ to 10^{-4} [55,37,53,38,51,39,45]. It is important to notice that the value of c_1 (in addition to p_{max} and the slope q), regulates the amount of flow kinetic energy that is transferred to the CRs. CR protons can be dynamically important by exerting a pressure

$$P_{cr} = \frac{4\pi}{3} \int_{p_{inj}}^{p_{max}} f(p) p^3 v dp = \frac{4\pi}{3} c \int_{p_{inj}}^{p_{max}} f(p) \frac{p^4}{(m_p^2 c^2 + p^2)^{1/2}} dp. \quad (45)$$

The ratio of the CR pressure to the ram pressure of the flow, $\rho_1 u_1^2$, can be regarded as a first order indication of the relative importance of the two components. For a flat CR distribution, i.e., $q \simeq 4$, which is typical of the cosmological case [5,28], by using the above expression for P_{cr} and neglecting the sub-relativistic contribution we find

$$\frac{P_{cr}}{\rho_1 u_1^2} = \frac{8}{3} \sqrt{\frac{2}{\pi}} c_1^3 e^{-2c_1^2} \left(\frac{m_p c}{p_{inj}}\right)^{3-q} \left(\frac{c}{u_s}\right)^2 \frac{\left(\frac{p_{max}}{p_{inj}}\right)^{4-q} - 1}{4-q} \quad (46)$$

Thus, for a CR ion component extending between 1 GeV and 10^6 GeV, ap-

proprate for shocks in galaxy clusters, the back-reaction of the accelerated particles would not be negligible with the aforementioned choices of the parameter c_1 . It appears that in cosmological simulations of large scale structure formation, most of the kinetic energy is processed by shocks with Mach number in the range 3-6 [9]. According to recent results from a newly developed Adaptive Mesh Refinement scheme with a resolution down to the diffusion length scale and capable of including self-consistently the dynamical role of the accelerated particles [56] shocks with Mach number $M \sim 3-6$ are expected to be “moderately” efficient (up to 30%) but not strongly modified. Thus, the effect of the back-reaction can be emulated by slightly increasing the value of c_1 , which has the effect of reducing the total number of injected CRs. For the above range of flow parameters, we find that a value of $c_1 = 2.6$ produces an injection efficiency η_{inj} consistent with above nonlinear calculations [56,57]. In general, however, one must be very cautious about the choice of c_1 . Its value should be determined on a individual basis, based on the properties of the simulated shocks where most of the CRs are being produced and in accord with the possible non-linear behavior of the shock acceleration mechanism there.

The physical process of injection of CR electrons is more complicated and basically not yet fully understood. Part of the reason is due to the fact that electrons carry only a small fraction of the momentum of the flow and, therefore, they do not affect the dynamics of the shock. Thus, unlike the ions, whose behavior can be constrained by general considerations of energy and momentum conservation, the electrons behave as test particles and their dynamics is determined by the details of the plasma wave-particle interactions. The latter is very difficult to model appropriately in computer simulations. In addition, until recently the observational results available in this respect were very limited. In this situation, the progress in the understanding of CR electron injection at shocks has been relatively slow. However, for the present purpose of a numerical treatment of CR injection at cosmic shocks, a viable and reasonable approach is to assume that the ratio of the cosmic ray electrons to ions at relativistic energies is fixed to a value $R_{e/p}$ [58]. This phenomenological approach is supported by some observational evidence from experiments with Galactic cosmic rays indicating that this ratio is possibly in the range 1-5 % [59,60].

3.6 Production of Secondaries

Electrons and ions injected at shocks provide the main source of CRs and are usually referred to as *primary*. As high energy protons propagate through the galactic or intergalactic medium, they collide with the background thermal protons and, from the hadronic interaction, secondary products are generated. The latter include photons, leptons and hadrons and, therefore, might

be an important source of relativistic electrons. The main channels for the production of secondary electrons (positrons) are [61]:

$$p + p \rightarrow \pi^\pm + X \quad (47)$$

$$p + p \rightarrow K^\pm + X. \quad (48)$$

where X indicates all the by products of the reactions. Charged pions decay with a lifetime of 2.6×10^{-8} s [62], mostly into

$$\pi^+ \rightarrow \mu^+ + \nu_\mu \quad (49)$$

$$\pi^- \rightarrow \mu^- + \bar{\nu}_\mu \quad (50)$$

Kaons, analogously, have a lifetime of 1.24×10^{-8} s and decay primarily into muons (63.5%) and pions (21.2%) [62]:

$$K^+ \rightarrow \mu^+ + \nu_\mu \quad (51)$$

$$K^- \rightarrow \mu^- + \bar{\nu}_\mu \quad (52)$$

$$K^\pm \rightarrow \pi^0 + \pi^\pm \quad (53)$$

The relative contributions of the two channels ($p + p \rightarrow \pi^\pm + X$ and $p + p \rightarrow K^\pm + X$) are energy dependent. So, for example, the fraction of secondary muons from K decay is 8% at about 100 GeV, 19% at 1 TeV and approaches asymptotically 27% at higher energy [61]. In turn, muons have a lifetime of 2.2×10^{-6} s [62] before decaying into

$$\mu^+ \rightarrow e^+ + \nu_e + \bar{\nu}_\mu \quad (54)$$

$$\mu^- \rightarrow e^- + \bar{\nu}_e + \nu_\mu. \quad (55)$$

In addition to $p + p$ inelastic collisions, the above cascades are also triggered by the interaction of $p + \text{He}$, $\alpha + \text{H}$ and $\alpha + \text{He}$, which, for example, increase the overall yield of secondary e^\pm by a factor 1.4 for a metal composition relative to the interstellar medium [63].

In general we can write the production spectrum of secondary electrons as [64]

$$j_s(\varepsilon_s) = n_H \sum_{i=\pi, K} \int_{\varepsilon_p^{min}}^{\infty} d\varepsilon_p J_p(\varepsilon_p) \langle \zeta \sigma_i(\varepsilon_p) \rangle \int_{\varepsilon_i^{min}(\varepsilon_s)}^{\varepsilon_i^{max}(\varepsilon_p)} d\varepsilon_i F_s(\varepsilon_s, \varepsilon_i) F_i(\varepsilon_i, \varepsilon_p) \quad (56)$$

where $J_p(\varepsilon_p)$ is the proton flux; $\langle \zeta \sigma_i(\varepsilon_p) \rangle$ is the inclusive cross section² of the processes (47) and (48); ε_p^{min} is the minimum proton energy required to produce a meson of energy ε_i^{min} and ε_i^{max} the maximal energy of the produced meson; ε_i^{min} in turn is the minimum required energy of a meson for production of secondaries of energy ε_s ; finally $F_i(\varepsilon_{\pi,K}, \varepsilon_p)$ are the spectra of π and K produced from the collision of a proton of energy ε_p and $F_s(\varepsilon_s, \varepsilon_{\pi,K})$ the distribution of secondaries from the subsequent decay of the above collision products. For a full summary of the technique employed here in calculating the cross sections and the functions F_s and F_i we refer to ref. [64].

3.7 Energy Losses

We have considered the energy losses due to a variety of physical mechanisms that become relevant at different energy regimes. For the electrons, the most effective process is due to Coulomb losses in the low energy end and synchrotron and inverse Compton emission at high energies. Bremsstrahlung losses are also included for completeness, although less relevant. For ion CRs, Coulomb losses, which are mechanical in nature, are dominant below relativistic energy. However, given the much smaller cross section for radiative losses for the ions ($\propto 1/m_p^2$) as compared to electrons ($\propto 1/m_e^2$), the next important loss mechanism for the CR ions beside adiabatic expansion is that due to inelastic collisions with the thermal background nuclei. In the following we shall provide the functions

$$b(p) \equiv \frac{dp}{dt} \quad (58)$$

and the associated cooling time

$$\tau_{cool} \equiv \frac{p}{b(p)} \quad (59)$$

relative to each relevant process, and separately for electrons and ions.

3.7.1 Electrons

Losses due to Coulomb collisions are expressed by [65]

² Inclusive means that which describes the process

$$p + p \rightarrow i + X \quad (57)$$

where i is in general a secondary particle

$$\begin{aligned}
\left(\frac{dp}{dt}\right)_{Coul} &= \frac{2\pi Z^2 e^4}{m_e c^2} n \left\{ \ln \left(\frac{m_e^3 c^4}{4\pi e^2 \hbar^2 Z} \right) + \ln \left[\frac{(1 + \hat{p}^2)^{1/2}}{n} \right] - \frac{3}{4} \right\} \\
&= 3.01 \times 10^{-29} \left\{ 1 + [\ln(1 + \hat{p}^2)^{1/2} - \ln n] \frac{1}{73.56} \right\} n \text{ erg cm}^{-1} \quad (60)
\end{aligned}$$

where Z is the electric charge of the ion species, n is the number density of the background gas in cm^{-3} and $\hat{p} \equiv p/m_e c$. Taking $Z = 1$, the corresponding cooling time is defined as

$$\tau_{Coul} = 2.53 \times 10^9 \left(\frac{\hat{p}}{100} \right) \left(\frac{n}{10^{-3} \text{cm}^{-3}} \right)^{-1} \text{ yr.} \quad (61)$$

Bremsstrahlung losses are defined as [66,65]

$$\begin{aligned}
\left(\frac{dp}{dt}\right)_{brem} &= 4\alpha_f r_e^2 \gamma m_e c^2 Z(Z+1) n \left[\ln(2\gamma) - \frac{1}{3} \right] \\
&= 3.8 \times 10^{-33} \left\{ \ln[2(1 + \hat{p}^2)^{1/2}] - \frac{1}{3} \right\} \hat{p} n \text{ erg cm}^{-1} \quad (62)
\end{aligned}$$

where α_f is the fine structure constant, r_e the classical electron radius. Such mechanism is basically unimportant as it becomes effective on a time-scale

$$\tau_{brem} = 6 \times 10^{12} \left(\frac{n}{10^{-3} \text{cm}^{-3}} \right)^{-1} \text{ yr,} \quad (63)$$

again taking $Z = 1$. The other relevant loss mechanisms for electrons are due to synchrotron emission and inverse Compton scattering off the cosmic microwave background photons. After averaging over the electrons pitch angle, their combined contribution is given by

$$\begin{aligned}
\left(\frac{dp}{dt}\right)_{sync+IC} &= \frac{4}{3} \frac{\sigma_T p^2}{m_e^2 c^2} (u_B + u_{cmb}) \\
&= 8.94 \times 10^{-25} (u_B + u_{cmb}) \hat{p}^2 \text{ erg cm}^{-1} \quad (64)
\end{aligned}$$

where U_B and $u_{cmb} = 4.2 \times 10^{-13} (1+z)^4$ are the energy density in magnetic field and cosmic microwave background at a given cosmological red-shift, z , respectively, both in units of erg cm^{-3} . For high energy electrons this is the most severe energy loss mechanism with a typical time-scale at red-shift $z = 0$

$$\tau_{sync+IC} = 2.3 \times 10^8 \left(\frac{\hat{p}}{10^4} \right)^{-1} \left(1 + \frac{u_B}{u_{cmb}} \right)^{-1} \text{ yr.} \quad (65)$$

3.7.2 Ions

Coulomb collisions are efficient at a rate [65]

$$\begin{aligned}
\left(\frac{dp}{dt}\right)_{Coul} &= \frac{2\pi Z^2 e^4}{m_e c^2} n \ln \left(\frac{\gamma^2 m_e^3 c^4}{\pi e^2 \hbar^2 n} \frac{m_p \beta^4}{m_p + 2\gamma m_e} \right) \frac{\beta^3}{x_m^3 + \beta^3} \\
&= 3.01 \times 10^{-29} \left\{ 1 + \left[\ln \left(\frac{\hat{p}^4 / (1 + \hat{p}^2)}{1 + 2(m_e/m_p)(1 + \hat{p}^2)^{1/2}} \right) - \ln n \right] \frac{1}{75.7} \right\} \cdot \\
&\quad \frac{\beta^3}{x_m^3 + \beta^3} n \text{ erg cm}^{-1}
\end{aligned} \tag{66}$$

where $\beta = v/c$,

$$x_m = \left(\frac{3\pi}{4}\right)^{1/3} \left(\frac{2kT_e}{m_e c^2}\right)^{1/2} = 6.4 \times 10^{-2} \left(\frac{T_e}{10^7 \text{K}}\right)^{1/2} \tag{67}$$

and we now define $\hat{p} \equiv p/m_p c$. For protons in the low energy end within the range considered here, Coulomb collisions are the only significant energy loss mechanism, with a time-scale comparable to the Hubble time,

$$\tau_{Coul} = 4.8 \times 10^9 \left(\frac{\hat{p}}{0.1}\right) \left(\frac{n}{10^{-3} \text{cm}^{-3}}\right)^{-1} \text{ yr}, \tag{68}$$

where $Z = 1$ is used. Photo-pair and photo-hadron production of CR ions A , interacting with the cosmic microwave background photons, i.e.,

$$A + \gamma_{cmb} \rightarrow A + e^+ + e^- \tag{69}$$

$$A + \gamma_{cmb} \rightarrow A + \pi \tag{70}$$

are mostly negligible at the energies we include. In fact, for red-shift $z = 0$ and taking the average CMB photon energy $\langle \epsilon_{cmb} \rangle = 7 \times 10^{-4} \text{eV}$, the thresholds for the above reactions, in terms of the Lorentz γ factor, are respectively

$$\gamma_{min} = \frac{m_e c^2}{\langle \epsilon_{cmb} \rangle} \simeq 7 \times 10^8 \tag{71}$$

$$\gamma_{min} = \frac{\xi m_\pi c^2}{2\langle \epsilon_{cmb} \rangle} \left(1 + \frac{\xi m_\pi}{2m_p}\right) \simeq \xi \times 10^{11} \tag{72}$$

reachable only for ultra high energy CRs (where ξ is the multiplicity of the produced pions). Rather, inelastic collisions of CR ions off nuclei of the thermal background gas are more significant, being at a rate [43]

$$\begin{aligned}
\left(\frac{dp}{dt}\right)_{p-p} &= \sigma_{\pi,inel}(E_p - m_p c^2)n \\
&= \begin{cases} 2.91 \times 10^{-29} (\hat{p} - \beta)n \text{ erg cm}^{-1} & \text{if } e_p \geq 1.22\text{GeV} \\ 0 & \text{if } e_p < 1.22\text{GeV} \end{cases}
\end{aligned} \tag{73}$$

and characterized by a energy loss time-scale

$$\tau_{p-p} = 5.5 \times 10^{10} \left(\frac{n}{10^{-3}\text{cm}^{-3}} \right)^{-1} \text{ yr} \tag{74}$$

4 Test Results of the Code

In the following we present a set of numerical experiments that test the performance of the code in various cases of direct interest. In particular we consider the time evolution of an initial distribution of CR protons and electrons as they lose energy subject to mechanisms described in §3.7. Alternatively, we also present the evolution toward the steady state of electrons which are continually injected as secondary products of p-p collisions and at the same time lose energy due to Coulomb and inverse Compton losses. For the first experiment we take the initial spectrum of the cosmic rays (protons and electrons) as a power-law with logarithmic slope $q_0 = 4.3$. A similar distribution (but with a different normalization) will also provide the parent CR protons that produce the secondary electrons in the last example. The numerical solution, which gives the number density of CRs in each momentum bin as a function of time, t , is plotted and compared with the analytical solution. The latter is obtained by integrating between each momentum bin bounds the exact, analytical CR distribution corresponding to the time t [67], for the same initial distribution evolved by the code. As for the Coulomb, bremsstrahlung and p-p collision losses, we assume that the CR protons or electrons propagate through a medium with number density $n_{gas} = 10^{-3}\text{cm}^{-3}$, typical of the core of clusters of galaxies. In order to further mimic cosmic conditions, the test are run for a time $\tau_H = 1.5 \times 10^{10}$ yr so that all the cooling time-scales of relevance in a cosmological simulation are included.

4.1 Evolution of Cosmic Ray Power-Law Distributions

In fig. 1 we present the temporal evolution of a distribution of CR protons subject to Coulomb losses and p-p inelastic collisions. For this experiment we use 8 momentum bins, with the CR spectrum extending between $p_0 = 0.1\text{GeV}/c$ up to $p_8 = 10^6\text{GeV}/c$ (c is the speed of light). The dis-

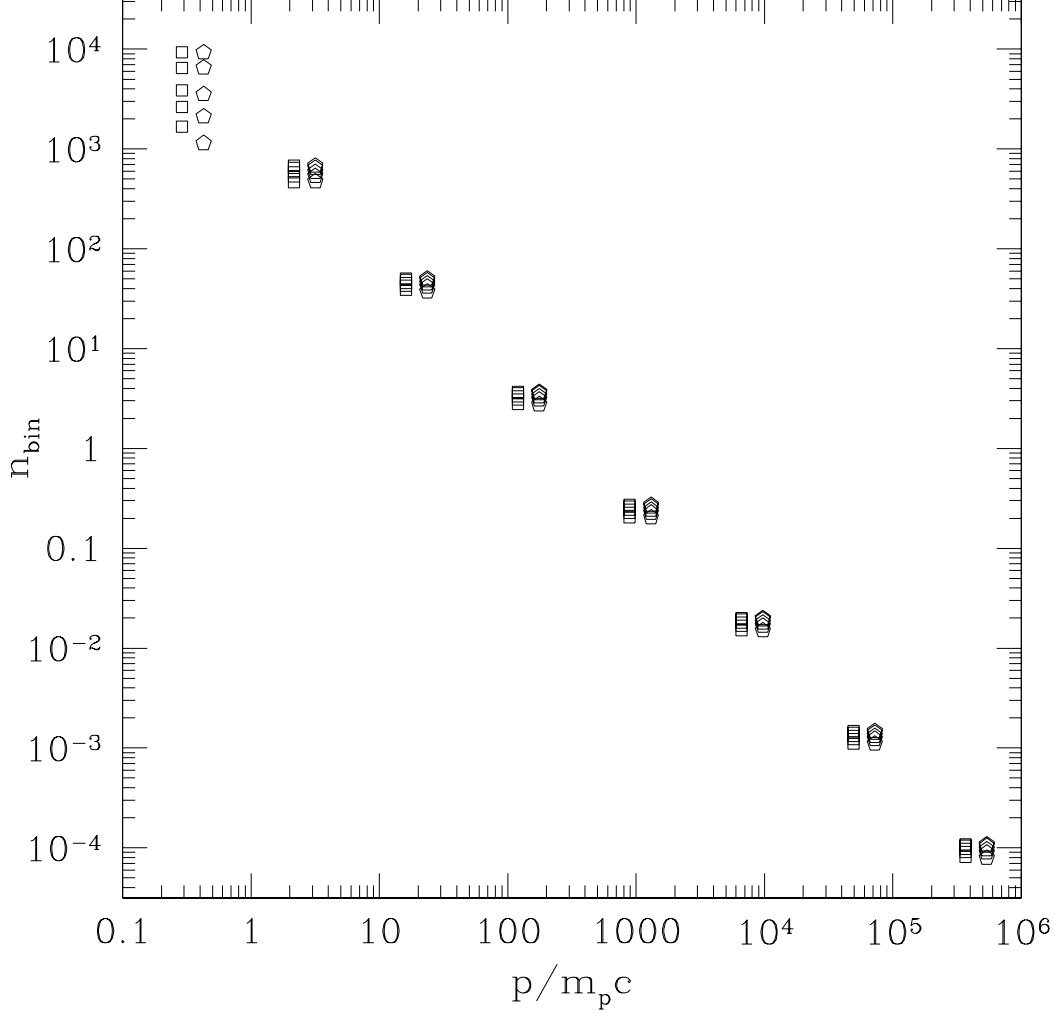


Fig. 1. Evolution of CR proton spectrum with initial logarithmic slope $q_0 = 4.3$, subject to Coulomb losses and p-p inelastic collisions over a period of 15 Gyr.

tance between subsequent bin bounds is constant on a logarithmic scale and is $\Delta w = [\log(p_8) - \log(p_0)]/8 = 0.875$. Since the losses are only mild in this case, the numerical evolution of the CRs is computed by the scheme presented in §3.1. For each momentum bin, on the ordinate axis we plot the number density of CR protons as computed from the code (pentagons) and from the analytical solution (square). Here and in the following figures, in order to facilitate the visual comparison of the results, for each bin the squares are drawn in correspondence of the middle of the bin and pentagons at a slightly higher momentum value, although the bins are identical for both cases. The points in the plot correspond to the following times $t/\tau_H = 0.1, 0.3, 0.5, 0.8, 1$. The time sequence is such that, for each bin, points in the upper positions correspond to earlier times. As we can see, above 1 GeV the CRs are only sensitive to the p-p losses which deplete all the momentum bins at the same rate. In this regime the two solutions, the numerical and the analytical one, are, for

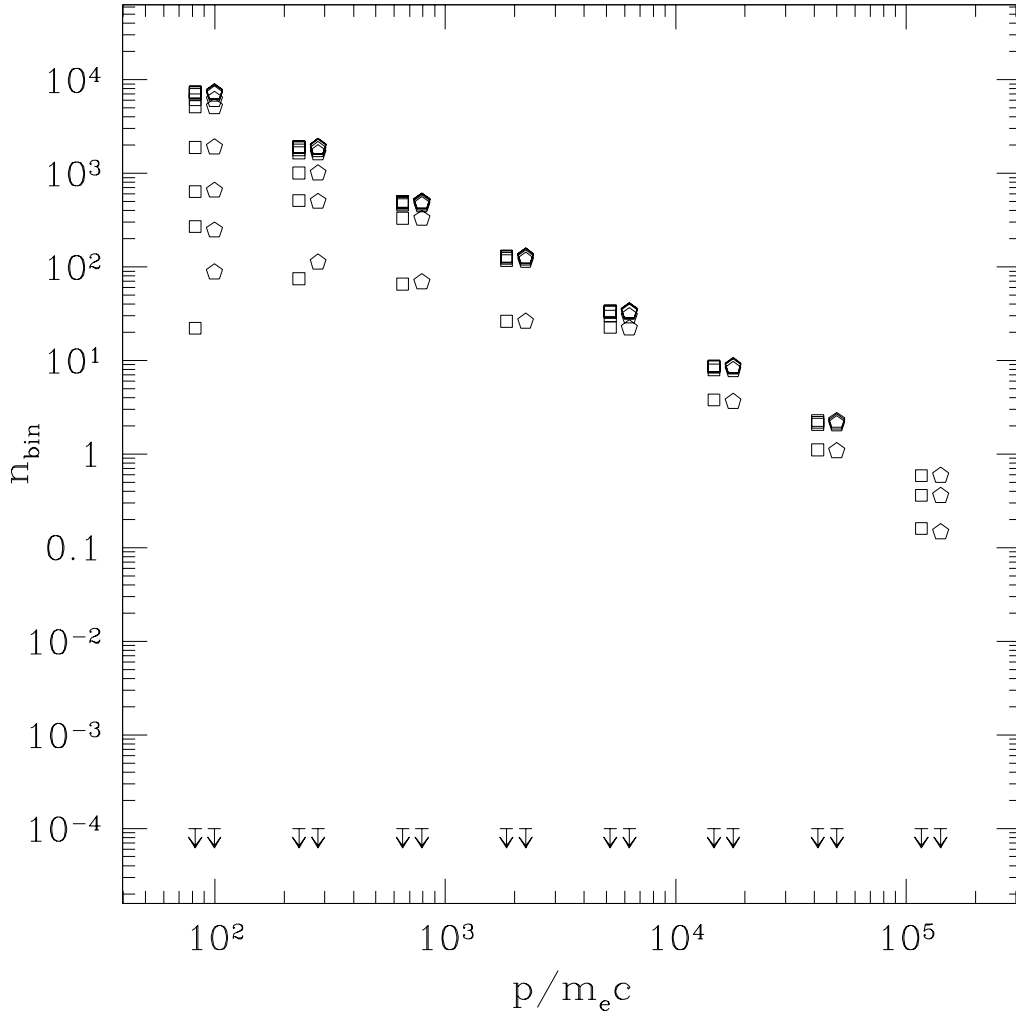


Fig. 2. Evolution of CR electron spectrum subject to Coulomb, bremsstrahlung and inverse Compton losses over a period of 15 Gyr. The initial logarithmic slope was set to 4.3

all practical purposes, identical. At lower energies, i.e., for the first bin, the numerical solution still follows very accurately the exact solution. Only in the last two points of the time sequence, after $t = 1.2 \times 10^{10} \text{yr} = 0.8 \tau_{\text{Coul}} (\hat{p}/0.3)$, the numerical solution cools a little bit faster than the analytical one and the number of CR protons in the first bin (only!) is slightly underestimated by a factor $\lesssim 1.4$.

Analogously, in Fig. 2, we present a comparison between the numerical (pentagons) and the analytical (square) solutions for the evolution of an initial power-law distribution of CR electrons. In this case, the numerical solution of the evolution of the CR distribution is computed by means of the more sophisticated (and more expensive) scheme outlined in §3.2. Again we use 8 momentum bins, but the extrema of the CR electrons spectrum are now

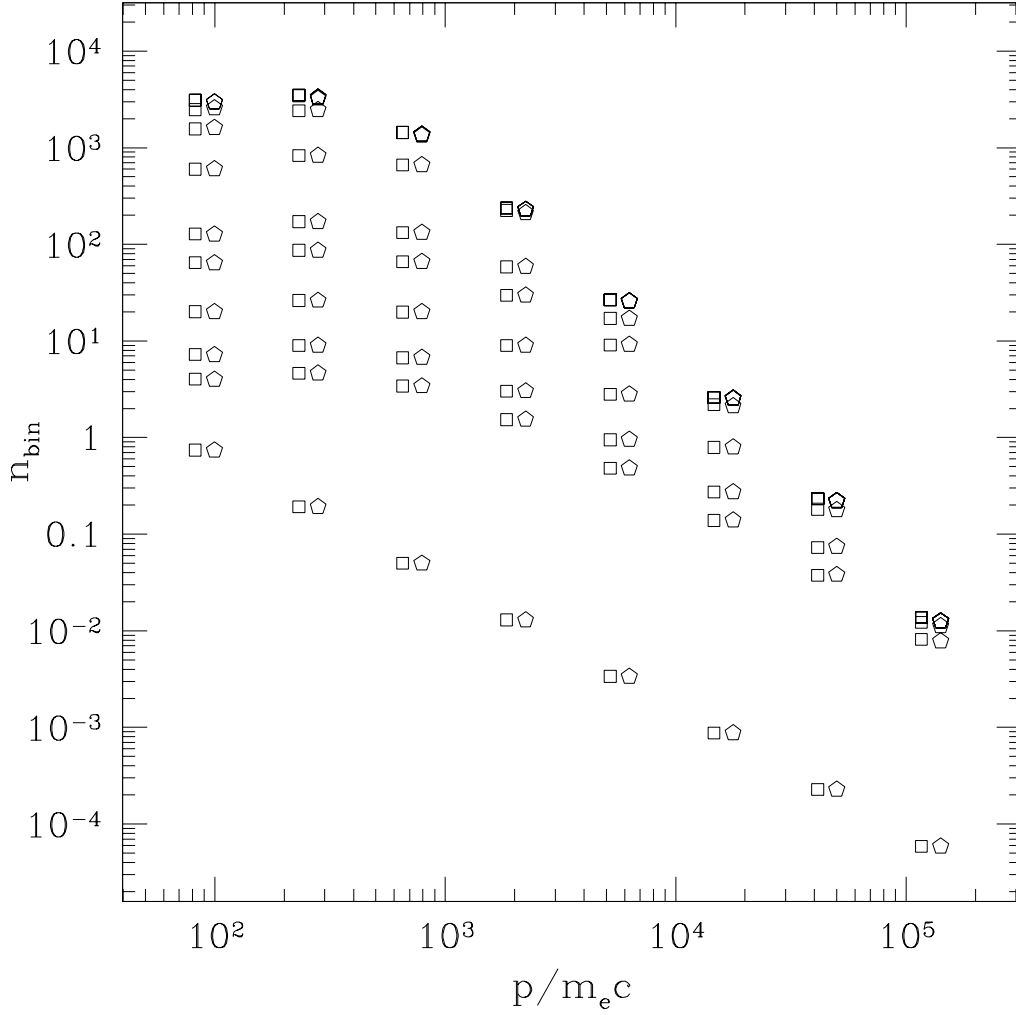


Fig. 3. Evolution of secondary CRs produced in p-p collision by a power-law distribution of parent CR protons with logarithmic slope was set to 4.3

$p_0 = 50\text{MeV}/c$ and $p_8 = 2 \times 10^5\text{MeV}/c$ with a distance between subsequent bin bounds $\Delta w = 0.45$. The inverse Compton losses are computed by setting $u_b \ll u_{cmb} = 4.2 \times 10^{-13}$. The values of the CR number density for each bin in Fig. 2 has been plotted for the following times (ages) of the distributions: $t/\tau_H = 5 \times 10^{-4}, 1 \times 10^{-3}, 3 \times 10^{-3}, 1 \times 10^{-2}, 2 \times 10^{-2}, 0.1, 0.25, 0.45, 0.6, .7$. The above times have been chosen in order to test the accuracy of the numerical routine in different regimes. For example, the first three times correspond to a fraction of $\tau_{IC+sync}$ for particles with $\hat{p} \simeq 10^4$, whereas the last times are a significant fraction of τ_{Coul} . Again, since the evolution of the CR spectrum is determined by energy losses, the time evolution is such that the upper points correspond to earlier stages. Since the cooling time for the CR electrons in the high energy bins is much shorter than the total evolution time τ_H , eventually such bins will be evacuated. Since the plotted dynamical range is limited, we

adopt “upper limit” symbols for those bins where cooling has reduced the number of particles below an arbitrary numeric level of 10^{-4} . We notice once again a very accurate correspondence between the code and the analytical solution. As for the CR protons, the numerical solution departs slightly from the analytical one at the lower energies (for the first 2 bins). However, this now takes place only after $t \geq 0.6 \tau_H = 7.1 \tau_{Coul}$, to be compared with $t \geq 0.8 \tau_{Coul}$ for the protons case. This means that the present scheme is more accurate not only for the evolution of the high energy part of the spectrum but also the low energy end. This feature is relevant in the context of cosmological simulations because the time-scales for the energy losses of electrons at all energies of interest are significantly shorter than a Hubble time. Notice that, unlike the previous case, the numerical solution now overestimates the total number of CRs in the lower momentum bins. The discrepancy, however, appears only when a momentum bin has already been significantly evacuated of electrons and is close to complete depletion. From Fig. 2 we can see that the difference between the true and the numerical solution (for both first and second bins) is only a small fraction of the difference between the initial and the current value. Also, notice that after the second momentum bin has been evacuated, i.e., around $t/\tau_H \sim 0.5$, the scheme is working with only one momentum bin.

Finally, in Fig. 3 we compare the numerical and analytical results for the evolution of a distribution of secondary CR electrons, continuously injected through the processes described in §3.6. In this case we start from a low background distribution of CR electrons and the continuous injection of new particles builds up the steady state distribution. Thus, unlike in the previous examples, now the time evolution is such that the lower points correspond to earlier times. The CR electron distributions have been plotted for both the numerical (pentagons) and analytical (square) solutions for the following times: $t/\tau_H = 5 \times 10^{-4}, 1 \times 10^{-3}, 3 \times 10^{-3}, 1 \times 10^{-2}, 2 \times 10^{-2}, 0.1, 0.3, 0.5, 0.8, 1$. Again the numerical scheme follows very precisely the evolution of the spectrum of the secondary electrons. Since the slope of the parent CR protons was $q_0 = 4.3$, the injection spectrum has a logarithmic slope $q_i = 4.3$ [43]. Thus, as expected, the slope of the steady state spectrum is respectively steeper at high energies and flatter at the low energy end than the injection spectrum by one unity. We notice, however, that the first and last bins are even flatter and steeper respectively than the above prediction. At low energies, this is a physical effect due to the reduction of the injection rates of secondary electrons as we approach the lower energy limit for electron production $\sim m_\mu/2 \sim 50\text{MeV}$ [68]. The steepening of the slope of the last bin, on the other hand, is a boundary effect, namely the lack of incoming flux of electrons from higher energies. This is due to the fact that we included an injection spectrum only up to electron energy of 100 GeV. Since the same injection spectrum was used for both the numerical and the analytical solutions, the test comparison is unaffected by this choice.

Fig. 4. Gray-scale image of a 2-D slice of the gas density distribution in units cm^{-3} for a cluster selected from the simulation. Linear size of the image is ca. $5 h^{-1}\text{Mpc}$.

4.2 Cosmic Ray Distributions in a Galaxy Cluster from a Cosmological Simulation

At last we present the distribution of CR protons as well as primary and secondary electrons, produced in a cosmological simulation of large scale structure formation performed by implementing COSMOCR into a hydro+N body cosmological code [69]. The simulations are described in detail elsewhere [5,27,28]. For the present purpose it suffices to mention that we assumed a Λ CDM cosmology with an initial power spectrum of density fluctuations with cluster normalization $\sigma_8 = 0.6$ and spectral index $n = 1$; normalized Hubble constant $h \equiv H_0/(100 \text{ km s}^{-1} \text{ Mpc}^{-1}) = 0.5$; total mass density $\Omega_M = 1$; and baryonic fraction $\Omega_b = 0.13$. For the simulation we selected a cosmological volume defined by a cubic region of comoving size $50 h^{-1}\text{Mpc}$ and use 256^3 cells for the baryonic matter and 128^3 dark matter particles. This corresponds to a spatial resolution of $\sim 200 h^{-1}\text{kpc}$. The CR protons and primary electrons have been injected and accelerated at shocks formed during the simulation with the prescription described in §3, whereas secondary electrons are produced in p-p collisions.

We have selected one of the clusters formed in the simulations. In Fig. 4 we show a gray-scale image of a slice of the gas density in units cm^{-3} through the core of such clusters. For the same cluster, in Fig. 5 (left panel) we present the analogous distribution of CR protons, and in Fig. 6 (left panels) that of primary (top) and secondary electrons (bottom) as well. In addition to the CR spatial distribution for each species we also project onto the corresponding right panel the CR *spectral* distribution (upper-half) and log-slope (lower-half) for two locations in the intra-cluster medium: the cluster center (open squares) and its periphery nearby an accretion shock (filled pentagons).

The spatial distribution of each species resembles that of the gas density. In

Fig. 5. Left: distribution of the total number density of CR protons in units of cm^{-3} . The length of a side of the image is $5 h^{-1}\text{Mpc}$. Right: number density (top) and power law index (bottom) for each momentum bin for two locations in the intra-cluster medium, at the cluster core (open squares) and periphery (filled pentagons).

Fig. 6. Same as in Fig. 5 but for primary (top panels) and secondary electrons (bottom panels).

addition, CRs are only present within the shocked regions. This makes sense because roughly speaking according to our injection mechanism the CR particles are generated downstream of shocks and are then passively advected with the flow. For the case of the protons (Fig. 5) the number density is higher in the cluster core (right panel - open squares) than in the periphery (right panel - filled pentagons) due to the adiabatic compression undergone by the CRs together with the gas during the formation of the cluster. And in fact, in the inner regions of the cluster where the gas is denser and, therefore, the Coulomb losses stronger, the CR proton spectrum shows a mild flattening at low energies (Fig. 5, right-panel bottom-section), with respect to the distribution in the outer region.

Analogously, the *total* number of CR primary electrons is larger at the cluster core than at its periphery (Fig. 6, left-top panel). However, at the high energy end the primary electrons in the cluster center have been completely depleted due to severe inverse Compton losses, unlike in the peripheral region behind the accretion shock where fresh CR electrons are being generated. Such difference is reflected also in the values of the log-slope of the distributions, steep for $\hat{p} \geq 10^3$ in the cluster center and still relatively flat at the periphery near the shock (Fig. 6, left-top panel). Finally, the bottom part of Fig. 6 shows the properties of CR secondary electrons. Again the number density is higher at the center of the cluster than at its outskirts. Notice that the number density of secondary electrons roughly scales as $n_p n_{gas} \propto n_p^2$. In fact, this qualitative difference is reflected, approximately in the right proportion, in the larger distance between the two density curves in the bottom right panel (upper-half) of Fig. 6, as compared to those in Fig. 5. Notice also that the log-slope of the distribution of the secondary spectrum is steeper (flatter) than that of the parent CR protons at high (low) energies by approximately one unit as expected. Again, the first and last bin make an exception to this expectation, in accord to our explanation in §4.1.

5 Conclusions

In this paper we described COSMOCR, a code for cosmic ray associated studies in cosmological simulations. We have described the scientific motivations behind such code, the challenges posed by the realization of a suitable algorithm and the various numerical schemes adopted here in order to follow the evolution of different CR species. We have shown in §4 that the present code is able to follow with high accuracy the evolution of a CR distribution of protons as well as primary and secondary electrons subject to the mechanisms of energy loss of interest in the intra-cluster medium. Additionally, COSMOCR has been implemented in a cosmological code [69]. The resulting distribution of CR populations are in accord with what we know about the properties of the

cosmic shocks responsible for the acceleration of such CRs [9], and with our knowledge of the transport and losses mechanism that regulate their evolution.

Acknowledgements

I am indebted to T. W. Jones, H. Kang and D. Ryu for valuable comments on the manuscript. I am also grateful to an anonymous referee for providing useful comments. I wish to acknowledge support from a Doctoral Dissertation Fellowship at the University of Minnesota and from a fellowship provided by the Research Training Network of the European Commission for the Physics of the Inter-galactic Medium. This work has been supported in part by NASA grant NAG5-5055, by NSF grants AST96-16964 and AST00-71167, by the University of Minnesota Supercomputing Institute and by the Max-Planck-Institut für Astrophysik.

References

- [1] N. A. Bahcall, J. P. Ostriker, S. Perlmutter, and P. J. Steinhardt, *Science* **284**, 1481 (1999).
- [2] S. D. M. White, J. F. Navarro, A. E. Evrard, and C. S. Frenk, *Nature* (London) **366**, 429 (1993).
- [3] J. P. Ostriker, *Ann. Rev. Astron. Astrophys.* **31**, 689 (1993).
- [4] P. J. E. Peebles, *Principles of Physical Cosmology* (Princeton University Press, Princeton New Jersey, 1993).
- [5] F. Miniati, Ph.D. thesis, University of Minnesota, 2000.
- [6] R. A. Sunyaev and Y. B. Zel'dovich, *Astr. Astrophys.* **20**, 189 (1972).
- [7] E. Bertschinger, *Astrophys. J. Suppl.* **58**, 39 (1985).
- [8] D. Ryu and H. Kang, *Mon. Not. R. Astron. Soc.* **284**, 416 (1997).
- [9] F. Miniati *et al.*, *Astrophys. J.* **542**, 608 (2000).
- [10] V. S. Berezinskii *et al.*, *Astrophysics of Cosmic Rays* (Elsevier, Amsterdam: North-Holland, 1991).
- [11] V. S. Berezinsky, P. Blasi, and V. S. Ptuskin, *Astrophys. J.* **487**, 529 (1997).
- [12] T. W. Jones, F. Miniati, D. Ryu, and H. Kang, in *High Energy Gamma-Ray Astronomy*, Vol. 558 of *AIP Conference Proceedings*, edited by F. A. Aharonian and H. J. Völk (American Institute of Physics: New York, Heidelberg, 2001), pp. 436–447.
- [13] K.-T. Kim, P. P. Kronberg, G. Giovannini, and T. Venturi, *Nature* (London) **341**, 720 (1989).
- [14] K.-T. Kim, P. P. Kronberg, P. E. Dewdney, and T. L. Landecker, *Astrophys. J.* **355**, 29 (1990).
- [15] G. Giovannini *et al.*, *Astrophys. J.* **406**, 399 (1993).
- [16] B. M. Deiss, W. Reich, H. Lesch, and R. Wielebinski, *Astr. Astrophys.* **321**, 55 (1997).
- [17] G. Giovannini and L. Feretti, *New Astronomy* **5**, 335 (2000).
- [18] R. Fusco-Femiano *et al.*, *Astrophys. J. Lett.* **513**, L21 (1999).
- [19] J. S. Kaastra *et al.*, *Astrophys. J. Lett.* **519**, L119 (1999).
- [20] R. Lieu *et al.*, *Astrophys. J. Lett.* **458**, L5 (1996).
- [21] R. Lieu *et al.*, *Science* **274**, 1335 (1996).

- [22] J. P. D. Mittaz, R. Lieu, and F. J. Lockman, *Astrophys. J. Lett.* **498**, L17 (1998).
- [23] R. Lieu, M. Bonamente, and J. P. D. Mittaz, *Astrophys. J. Lett.* **517**, L91 (1999).
- [24] S. Bowyer, T. W. Berghoefer, and E. Korpela, *Astrophys. J.* **526**, 592 (1999).
- [25] M. Bonamente, R. Lieu, and J. P. Mittaz, *Astrophys. J.* **546**, 805 (2001).
- [26] T. W. Berghoefer, S. Bowyer, and E. Korpela, *Astrophys. J.* **535**, 615 (2000).
- [27] F. Miniati, T. W. Jones, H. Kang, and D. Ryu, *Astrophys. J.* (2001), submitted.
- [28] F. Miniati, D. Ryu, H. Kang, and T. W. Jones, *Astrophys. J.* **559**, 1 (2001), in press.
- [29] J. Skilling, *Mon. Not. R. Astron. Soc.* **172**, 557 (1975).
- [30] J. A. Peacock, *Mon. Not. R. Astron. Soc.* , **196**, 135 (1981).
- [31] A. L. Drury, *Mon. Not. R. Astron. Soc.* **235**, 997 (1988).
- [32] J. K. A. W. G. Y. G. Achterberg, *Astrophys. J.* **542**, 235 (2000).
- [33] R. G. Stone and B. T. Tsurutani, *Collisionless Shocks in the Heliosphere: A tutorial Review* (Am. Geophys. Union, Washington D.C., 1985).
- [34] B. T. Tsurutani and R. G. Stone, *Collisionless Shocks in the Heliosphere: Reviews of Current Research* (Am. Geophys. Union, Washington D.C., 1985).
- [35] D. C. Ellison, E. Moebius, and G. Paschmann, *Astrophys. J.* **352**, 376 (1990).
- [36] H. Kang and T. W. Jones, *Mon. Not. R. Astron. Soc.* **249**, 439 (1991).
- [37] T. W. Jones and H. Kang, *Astrophys. J.* **402**, 560 (1993).
- [38] E. G. Berezhko, V. K. Yelshin, and L. T. Ksenofontov, *Astropart. Phys.* **2**, 215 (1994).
- [39] E. G. Berezhko, V. K. Yelshin, and L. T. Ksenofontov, *Astronomy Reports* **40**, 155 (1996).
- [40] L. O. Drury, *Rep. Prog. Phys.* **46**, 973 (1983).
- [41] T. W. Jones, D. Ryu, and A. Engel, *Astrophys. J.* **512**, 105 (1999).
- [42] J. P. Ostriker and R. Cen, *Astrophys. J.* **464**, 27 (1996).
- [43] K. Mannheim and R. Schlickeiser, *Astr. Astrophys.* **286**, 983 (1994).
- [44] L. O. Drury, *Mon. Not. R. Astron. Soc.* **251**, 340 (1991).
- [45] E. G. Berezhko and D. C. Ellison, *Astrophys. J.* **526**, 385 (1999).
- [46] N. S. Kardashev, *Soviet Astron.-AJ* **6**, 317 (1962).

- [47] C. L. Sarazin, *Astrophys. J.* **520**, 529 (1999).
- [48] B. van Leer, *Toward the ultimate conservative difference scheme I. The quest of monotonicity, Lecture Notes in Physics* (Springer, Verlag, 1973).
- [49] G. Strang, *SIAM J. Num. Anal.* **5**, 506 (1968).
- [50] S. K. Godunov, *Mat. Sb.* **47**, 271 (1959).
- [51] M. A. Malkov and H. J. Völk, *Astr. Astrophys.* **300**, 605 (1995).
- [52] M. A. Malkov and H. J. Völk, *Adv. Space Res.* **21**, 551 (1998).
- [53] H. Kang and T. W. Jones, *Astrophys. J.* **447**, 994 (1995).
- [54] M. A. Lee, *J. Geoph. Res.* **87**, 5063 (1982).
- [55] L. O. Drury, W. J. Markiewicz, and H. J. Völk, *Astr. Astrophys.* **1989**, 179 (1989).
- [56] H. Kang, T. W. Jones, R. J. LeVeque, and K. M. Shyue, *Astrophys. J.* **550**, 737 (2001).
- [57] E. G. Berezhko, L. T. Ksenofontov, and V. K. Yelshin, *Nucl. Phys. B (Proc. Suppl.)* **39A**, 171 (1995).
- [58] D. C. Ellison, E. G. Berezhko, and M. G. Baring, *Astrophys. J.* **540**, 292 (2000).
- [59] D. Mueller and K.-K. Tang, *Astrophys. J.* **312**, 183 (1987).
- [60] D. Mueller and et al., in *Int. Cosmic Ray Conference* (PUBLISHER, Rome, 1995), Vol. 3, p. 13.
- [61] T. K. Gaisser, *Cosmic Rays and Particle Physics* (Cambridge University Press, Cambridge, 1990).
- [62] D. Groom *et al.*, *The European Physical Journal* **C15**, 1 (2000).
- [63] C. D. Dermer, *Astr. Astrophys.* **157**, 223 (1986).
- [64] I. V. Moskalenko and A. W. Strong, *Astrophys. J.* **493**, 694 (1998).
- [65] A. W. Strong and I. V. Moskalenko, *Astrophys. J.* **509**, 212 (1998).
- [66] V. L. Ginzburg, *Theoretical Physics and Astrophysics, International Series in Natural Philosophy* (Pergamon, Oxford, 1979).
- [67] V. L. Ginzburg and S. I. Syrovatskii, in *The Origin of Cosmic Rays*, edited by D. Ter Haar (Pergamon, Oxford, 1964).
- [68] M. Bardon and et al., *Phys. Rev. Lett.* **14**, 449 (1965).
- [69] D. Ryu, J. P. Ostriker, H. Kang, and R. Cen, *Astrophys. J.* **414**, 1 (1993).

This figure "figes.jpg" is available in "jpg" format from:

<http://arXiv.org/ps/astro-ph/0105447v1>

This figure "figp.jpg" is available in "jpg" format from:

<http://arXiv.org/ps/astro-ph/0105447v1>

This figure "nrho.jpg" is available in "jpg" format from:

<http://arXiv.org/ps/astro-ph/0105447v1>